

Enhancing Brain Source Reconstruction through Physics-Informed 3D Neural Networks

Marco Morik^{*1,2}, Ali Hashemi^{1,2}, Klaus-Robert Müller^{1,2,3,4}, Stefan Haufe^{5,6,7} and Shinichi Nakajima^{*1,2,8}

Abstract—Reconstructing brain sources is a fundamental challenge in neuroscience, crucial for understanding brain function and dysfunction. Electroencephalography (EEG) signals have a high temporal resolution. However, identifying the correct spatial location of brain sources from these signals remains difficult due to the ill-posed structure of the problem. Traditional methods predominantly rely on manually crafted priors, missing the flexibility of data-driven learning, while recent deep learning approaches focus on end-to-end learning, typically using the physical information of the forward model only for generating training data. We propose the novel hybrid method 3D-PIUNet for EEG source localization that effectively integrates the strengths of traditional and deep learning techniques. 3D-PIUNet starts from an initial physics-informed estimate by using the pseudo inverse to map from measurements to source space. Secondly, by viewing the brain as a 3D volume, we use a 3D convolutional U-Net to capture spatial dependencies and refine the solution according to the learned data prior. Training the model relies on simulated pseudo-realistic brain source data, covering different source distributions. Trained on this data, our model significantly improves spatial accuracy, demonstrating superior performance over both traditional and end-to-end data-driven methods. Additionally, we validate our findings with real EEG data from a visual task, where 3D-PIUNet successfully identifies the visual cortex and reconstructs the expected temporal behavior, thereby showcasing its practical applicability.

Index Terms—Deep Learning, EEG, Inverse Problem, Neuroimaging, Source Localisation

I. INTRODUCTION

To understand both normal brain function and dysfunction, it is essential to accurately identify the precise sources of electrical activity within the brain, a process known as *source localization* [1]. This is an important tool in cognitive neuroscience, enabling the study of brain responses to various stimuli and the functional organization of the brain. Electroencephalography (EEG) and magnetoencephalography (MEG) are non-invasive techniques that allow for monitoring brain activity without the need for surgical intervention [2]. Moreover,

This work was funded by the German Federal Ministry of Education and Research under the grant BIFOLD24B.

* Corresponding authors: m.morik@tu-berlin.de, nakajima@tu-berlin.de

1: The Berlin Institute for the Foundations of Learning and Data, Berlin, Germany

2: Machine Learning Group, Department of Computer Science, TU Berlin, Berlin, Germany

3: Department of Artificial Intelligence, Korea University, Seoul 136-713, Korea

4: Max Planck Institut für Informatik, Saarbrücken, Germany

5: Bernstein Center for Computational Neuroscience, Berlin, Germany

6: Physikalisch-Technische Bundesanstalt, Berlin, Germany

7: Berlin Center for Advanced Neuroimaging, Charité–Universitätsmedizin Berlin, Germany

8: RIKEN AIP, Tokyo, Japan.

M/EEG offers high temporal resolution, capturing neural events on the order of milliseconds, which is critical for studying fast neural dynamics and the timing of cognitive processes. This high temporal resolution makes EEG particularly suitable for investigating the rapid neural processes underlying cognition, perception, and action.

However, pinpointing the precise brain regions responsible for these signals remains a challenge due to the ill-posed nature of the EEG inverse problem [3]. Conventional methods try to address this by posing priors on the source activation, like sparsity or minimal norm activity [4]. Manual crafted priors bias the solution to specific settings. For example sparse methods do not work on distributed sources and minimum norm methods do not work for sparse sources. In recent years, neural networks [5]–[8] have shown improved performance by learning a direct mapping from the measurement to sources in an end-to-end fashion. Unlike traditional techniques, neural networks offer greater flexibility in formulating priors on brain activation by simulated data, that serves as a proxy for real-world conditions, possibly capturing a wide range of brain activity patterns. However, these approaches typically incorporate the forward model information only indirectly through their training data, which can limit their accuracy and generalizability in different contexts [9].

To combine worlds, we propose a novel hybrid approach, named 3D-PIUNet, that combines the strengths of both classical and deep learning methods. We incorporate physics-informed prior knowledge from the forward model via the pseudo-inverse solution provided by eLORETA [10]. Our method leverages a 3D convolutional neural network to refine this pseudo-inverse solution according to a learned data-driven prior that is able to capture complex patterns in the source space. We show a comparison of classical approaches, end-to-end learning and our proposed 3D-PIUNet in Fig. 1.

Our experimental results on a comprehensive synthetic dataset demonstrate that 3D-PIUNet consistently outperforms both eLORETA and end-to-end deep learning methods in terms of source localization accuracy. The network effectively learns to refine the pseudo-inverse solution, leading to more accurate and robust reconstructions, especially in the presence of noise. This work highlights the potential of best-of-both-worlds approaches to overcome the limitations of traditional and data-driven end-to-end methods in EEG source imaging.

To summarize our contribution, we

- propose the hybrid approach 3D-PIUNet that includes the physics information of the forward model into the deep learning framework via its pseudo inverse,

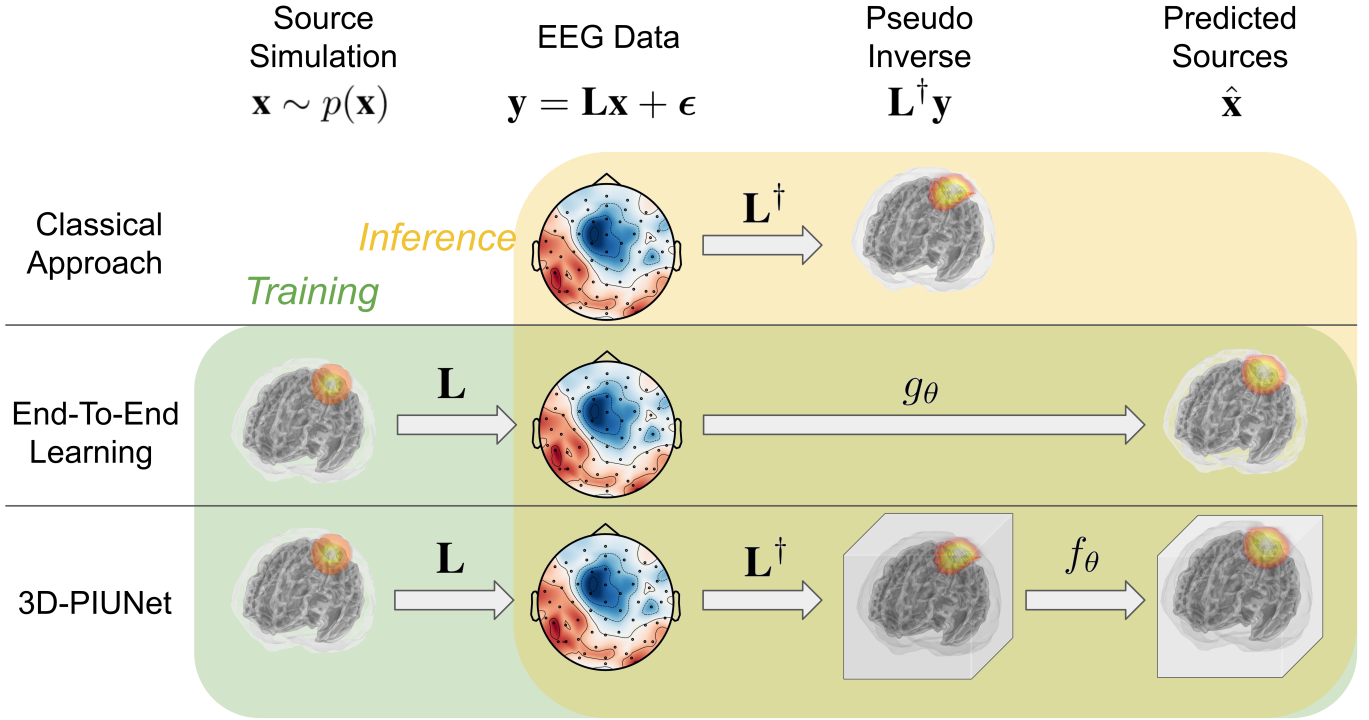


Fig. 1: Overview of different approaches for source localization from EEG data. **Top** The classical (Minimum Norm) approaches uses the pseudo-inverse \mathbf{L}^\dagger of the forward model to estimate the sources $\hat{\mathbf{x}}$ from the EEG measurements \mathbf{y} . **Middle:** Data-driven end-to-end approaches train some neural network g_θ on simulated data, where the source activity \mathbf{x} is drawn from the data prior $p(\mathbf{x})$. During inference, the network predicts the sources $\hat{\mathbf{x}}$ directly from measurements without explicitly using the forward model. **Bottom:** Our approach, 3D-PIUNet, integrates data-driven learning with physics-informed modeling by incorporating the forward model’s physical information through the pseudo-inverse. After transforming the EEG measurements into a grid-like source space, a 3D convolutional U-Net f_θ refines the pseudo-inverse solution according to the learned data prior, resulting in an improved source estimate $\hat{\mathbf{x}}$.

- demonstrate the benefits of 3D convolution in source space to learn the spatial patterns, and
- extensively benchmark our approach on diverse settings, showing superiority to both classical methods and end-to-end approaches across different signal-to-noise levels, number and size of sources.

II. BACKGROUND AND RELATED WORK

A. Problem Setup

EEG source localization aims to identify the spatial origins of electrical activity within the brain from scalp-recorded EEG signals. The mapping from brain sources to EEG measurements can be described by a linear *forward model*:

$$\mathbf{y} = \mathbf{L}\mathbf{x} + \epsilon, \quad (1)$$

where a known lead field matrix $\mathbf{L} \in \mathbb{R}^{M \times N}$ maps the electrical activity of the brain, $\mathbf{x} \in \mathbb{R}^{N \times T}$, to the sensor measurements, $\mathbf{y} \in \mathbb{R}^{M \times T}$. Here, M describes the number of sensors on the scalp, N the number of potential brain sources within the brain and T the number of time steps. The *noise vector* ϵ describes the measurement noise, covering inaccuracies in the forward model, electrical pollution and sensor errors.

The goal of source localization is to invert this forward model, therefore the name *inverse problem*. As $N \gg M$, the problem is

ill-posed, there are infinitely many possible solutions for a given set of measurements [11]. Therefore, finding a unique solution requires heavy regularization. By introducing reasonable priors over the source activation, the most likely source activation can be localized more accurately [1]. The different methods for source localization can be broadly categorized based on the assumed priors to constrain the infinite solution space.

B. Classical Approaches to EEG Source Localization

Early works on source localization assumed a limited and fixed number of sources active in the brain as a prior. In this dipole fitting both the position and orientation of the sources are adjusted to match the measurements [12], [13]. However, the number of active regions must be set in advance and the optimization problem becomes hard when trying to localize more than two dipoles.

On the other hand, distributed methods assume that brain activity can be spread across regions involving multiple dipoles. These methods place a dense set of potential source locations within the head volume. The inverse problem becomes a regularized regression problem, predicting the amplitudes of each location, thus not constraining the number of dipoles [14]. The Minimum Norm Estimates (MNE) [4] estimates the distribution of sources by minimizing the ℓ_2 -norm of the

source amplitudes. The ℓ_2 -norm offers a closed-form solution and is, therefore, fast to compute. However, it has a bias towards sources close to the sensors. To counteract this bias, different weighted minimum norm solutions [15] have been proposed, such as dSPM [16], LORETA [17], sLORETA [18] and eLORETA [10] or combinations of those [19]. As this weighting promotes a spatial smoothness prior, small sources might be missed or blurred. To obtain sparse solution with minimal non-zero sources, one can replace the ℓ_2 -norm with ℓ_1 -norm, called Least Absolute Shrinkage and Selection Operator (LASSO) [20] or selective minimum norm [21]. By combination of sparse and dense prior, it is also possible to generate solutions with mixed spatial extent [22].

Lastly, Bayesian frameworks integrate prior knowledge about source distributions to flexibly model brain activity [23]. Sparse Bayesian Learning (SBL) pioneered this approach by optimizing a Type-II ML cost function to enhance source estimation in noisy environments [24]. Building on SBL, hierarchical Bayesian inference techniques have extended this framework to simultaneously estimate both sources and noise addressing various noise structures, including homoscedastic [25], heteroscedastic [26], and full-structure [27] noise. These methods have been further extended to include coherent spatial source clusters as in cMEM [28].

C. Deep Learning Methods

In recent years, learning-based approaches have become popular in the sciences due to their flexibility and fast inference time, including EEG data analysis [29]. A better understanding of brain activity due to virtual brain models [30] and large-scale dynamical models [31] allow the generation of realistic simulation data acting as a powerful data-prior. To learn this data prior, previous work focused on end-to-end learning with different network architectures. For single timestep predictions, fully connected networks have been used to predict source locations directly [32], [33] showing the same limitation in fixed number of sources as dipole fitting. Convolutional networks have been proposed to encode spatial correlation of sensor measurement [7], mixing EEG and MEG signals [34] or to incorporate the time dimension [35]. Other recent approaches use LSTMs for temporal predictions after encoding the measurements either with residual networks [6], graph convolutional networks [36], dilated convolution [37] or multi-head attention [38]. However, all these end-to-end methods use the forward model only during data generation and require retraining or fine-tuning when the forward model changes [9]. Physics-informed machine learning bridges the gap and has shown superior performances in fields like fluid dynamics [39], quantum chemistry [40], quantum circuits [41], and other inverse problems like Computed Tomography (CT) [42] and MRI [43]. In the following, we explain our hybrid approach 3D-PIUNet for source localization, combining the benefits of classical and deep learning methods.

III. METHOD

Instead of learning the relationship between measurements and brain sources end-to-end, we propose a spatial-aware

neural network 3D-PIUNet to refine the eLORETA pseudo-inverse solution. This approach leverages a data prior while simplifying the problem by incorporating physical knowledge from the forward model. In the following, we first describe the benefit of starting from the pseudo-inverse, introduce the novel 3D convolutional network architecture and lastly explain the training paradigm that allows for accurate source reconstruction.

A. Starting from Pseudo-Inverse Solution

Previous works using neural networks for source estimation [6], [7], [38] learn a mapping $\hat{\mathbf{x}} = g_\theta(\mathbf{y}) : \mathbb{R}^M \rightarrow \mathbb{R}^N$ from sensor to source space. Even though this end-to-end learning is common practice in modern deep learning, it has some drawbacks for inverse problems. Most importantly, the model needs to learn the physical dynamics only from data, while not having access to a forward model. Therefore, the learned model heavily depends on the lead fields used during training and cannot generalize well to other forward models. For example, when the number of sensors change, classical end-to-end networks require the training of a new input layer.

We tackle these shortcomings by starting from a pseudo-inverse solution that maps the measurements to the source space. This way, the network can leverage the established physical knowledge embedded in the forward model. Importantly, as long as the pseudo-inverse matrix maintains full column rank, this transformation ensures that no information is lost. During training, the model learns a data prior in source space and can focus on refining the pseudo-inverse solution according to this prior. While this framework has been applied to other inverse problems like CT [42] and MRI [43] reconstruction, to the best of our knowledge, it is the first application to EEG data. Given the pseudo-inverse \mathbf{L}^\dagger , the neural network is trained using the transformed measurements $\tilde{\mathbf{x}} = \mathbf{L}^\dagger \mathbf{y}$ as an input. It then learns the refinement task as a mapping within source space $f_\theta : \mathbb{R}^N \rightarrow \mathbb{R}^N$:

$$\hat{\mathbf{x}} = f_\theta(\mathbf{L}^\dagger \mathbf{y}) \quad (2)$$

One can interpret the pseudo-inverse solution as a non-learnable physics-informed input layer that precedes the deep neural network. This way, the pseudo-inverse can be adapted to account for different subjects at inference time. By mapping the measurements into the source space, the input dimensionality does not depend on the sensing system and the same architecture can be used, enabling transfer learning.

Our framework is general in the sense that it works with different pseudo-inverse solutions as a starting point. While we propose the use of eLORETA, we also compared it with various pseudo-inverse solutions including MNE, sLORETA, dSPM, beamformer from the MNE package [44], as well as the Moore-Penrose inverse, identifying ℓ_2 -norm based methods, particularly eLORETA, performing best. The superiority of eLORETA might be due to its zero-localization error for single sources by compensating in the computation of the pseudo-inverse matrix \mathbf{L}^\dagger for depth and noise. We used a python implementation based on the MEG & EEG - Toolbox of Hamburg¹ with 0.05 regularization strength to compute the

¹(METH, Version: April 15, 2019) https://www.uke.de/dateien/institute/neurophysiologie-und-pathophysiologie/downloads/meth_2019_04.zip

eLORETA pseudo inverse.

B. 3D Convolution

We divide the brain sources to a regular 3D grid. This allows the use of a 3D convolutional neural network (CNN) [45]. CNNs excel in this domain due to their parameter efficiency and ability to capture spatial relationships. For tasks like source localization, where preserving spatial information across scales is crucial, the U-Net architecture [46] is particularly well-suited. It employs residual connections between the encoding (downscaling) and decoding (upscaling) blocks, allowing information from the input to propagate directly to the decoder and aiding in the reconstruction of fine details. For this work, we adopt a state-of-the-art U-Net architecture used in denoising diffusion models [47].

Before applying the network to our pseudo sources \tilde{x} , we use zero padding, extending the potential source locations to a regular $32 \times 32 \times 32$ grid. The architecture begins by lifting the pseudo inverse to a $C = 32$ channel feature map, effectively creating multiple representations of the initial source estimate. Next, the network progressively down-samples to a bottleneck resolution of $(8 \times 8 \times 8)$ while doubling the feature channels after each down convolution, increasing the receptive field of each convolutional layer. At each resolution, we use two 3D convolutional residual blocks. Each residual block starts with a Group Norm layer [48], a normalization technique that is less dependent on batch size, leading to improved training stability and performance. This is followed by SiLU activation, a smooth, non-linear activation function outperforming ReLU for deep neural networks [49]. The core computation is done by the $3 \times 3 \times 3$ convolution layers that aggregates neighboring information to learn descriptive features and refine the source estimates. Each block uses residual connections, where the input of each block is added to its output. This improves the gradient flow during backpropagation and simplifies the optimization problem [50].

At the bottleneck, we employ attention layers [51]. In contrast to Vision Transformers [52] that represent a group of pixels as a single token, we use a token for each voxel, but in low-resolution embedding space. The attention mechanism allows the model to focus on the most relevant regions for source reconstruction. These lower layers of the network capture a broader spatial context, and attention allows the model to weigh the importance of different regions within this context, leading to more accurate refinement of the source estimates.

Overall, the architecture incorporates a learned data prior, enabling refinement of the pseudo-inverse solution. We will show in the experiment section V, that this architecture improves the accuracy of source reconstruction in comparison to end-to-end models.

C. Training Details

To train 3D-PIUNet, we explored several loss functions proposed in the literature. Classical methods, like minimum norm estimates, typically optimize the mean squared error loss in measurement space [4]. However, this approach often

overfits to noise, particularly in low SNR conditions, where noise dominates the signal. Since we train with simulated data, we have access to paired signal and source data (y, x) , allowing us to compute the loss in noise-free source space. While related work has used cosine similarity [53] or ℓ_2 -loss in source space [6], we found the mean absolute error (ℓ_1) to be a more suitable option:

$$\text{Loss}(\mathbf{x}, f_{\theta}(\mathbf{L}^{\dagger}\mathbf{y})) = \|\mathbf{x} - f_{\theta}(\mathbf{L}^{\dagger}\mathbf{y})\|_1 \quad (3)$$

Compared to ℓ_2 -loss, ℓ_1 -loss is less sensitive to outliers, which is crucial in source reconstruction as outliers can arise from various sources, such as artifacts or model mismatches. The ℓ_1 -loss helps prevent these outliers from disproportionately influencing the learning process. Additionally, source activity is often sparse, meaning that only a few brain regions are actively generating signals at any given time. The ℓ_1 -loss encourages the model to learn sparse solutions, aligning with this prior knowledge about brain activity.

We used the Adam optimizer [54] with a learning rate of 0.00001 and a batch size of 32. The training process consisted of 60000 steps, where the data is generated via the simulation explained in section IV-B.

IV. EXPERIMENTAL SETUP

In this section, we describe how the training and testing data for the neural network was generated and introduce the performance metrics for evaluation.

A. Forward Model

To compute the forward model, we employ a three-shell Boundary Element Method (BEM) [55] approach implemented within the MNE-Python library [56]. To represent potential sources of brain activity, a volumetric source space is constructed. This source space consists of a three-dimensional grid with a uniform voxel spacing of 7 mm. The fsaverage [57] head geometry is used with three concentric layers representing the scalp, skull, and brain tissues and standard conductivity values assigned to these layers: $0.3S/m^2$ (scalp), $0.006S/m^2$ (skull), and $0.3S/m^2$ (brain). These values are based on established studies that provide realistic approximations for human head tissues [7].

To calculate the forward solution, the minimum distance between potential sources and the inner skull surface is set to 5 mm. This parameter helps exclude source locations that are unrealistically close to the skull boundary, resulting in $N = 4819$ sources. The volumetric source space is constructed with freely oriented sources, allowing each voxel to represent neural activity with a three-dimensional vector for direction and amplitude, providing greater flexibility in modeling complex neural activity patterns. Sensor positions are defined using a standard Easycap-M10 montage with $M = 61$ sensors. The resulting lead field matrix $\mathbf{L} \in \mathbb{R}^{(61 \times (4819 \cdot 3))}$ describes the mapping from source locations and orientation to sensors.

As using the same model for both forward and inverse solutions can lead to over-optimistic results — the so-called inverse crime [58], [59] — we generate a second BEM solution for testing. Here, the conductivity is changed to $0.332S/m^2$

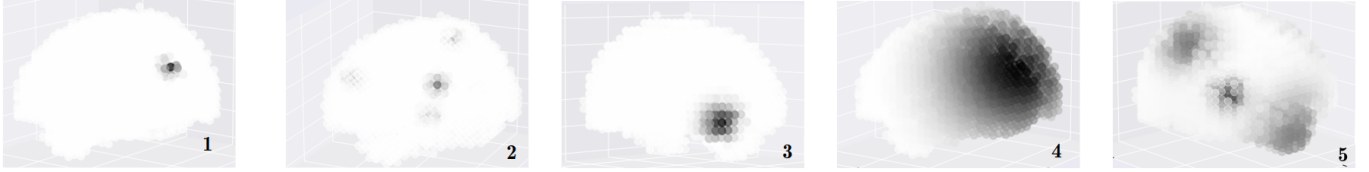


Fig. 2: We generate a diverse setting of brain activation. From left to right, we have **1.** a single active source with minimal width (10mm), **2.** 4 active sources with minimal width, **3.** a single medium-sized (20mm) active source, **4.** a single large active source (80mm), and **5.** a diverse sample with 4 active sources of different size, where two sources are partly overlapping.

(scalp), $0.0113S/m^2$ (skull), and $0.332S/m^2$ (brain) following an established setup [7], [60]. This ensures that our models are validated against a different forward model, simulating more realistic conditions and enhancing the robustness of our validation process.

B. Data Generation

We employ a controlled synthetic EEG data generation process to facilitate model evaluation with known ground truth. To isolate the spatial reconstruction aspect of the problem, we simulate source activation at a single point in time. The source activations are modeled as 3-dimensional Gaussian bell curves centered at random locations c within the brain. The width of each activation σ is given by the standard deviation of the bell curve. This allows us to simulate both localized and diffuse patterns of brain activity. Sources are assigned random orientations \vec{v} and their maximal amplitudes $a \sim \mathcal{N}(0, 1)$ is sampled from a standard normal distribution. We sample $S \sim \mathcal{U}(1, N_{\text{Activ}})$ distributed sources for a single data point. So given the center c_s , amplitude a_s and direction \vec{v}_s , we can calculate the activation of each source \mathbf{x}_i by the sum of the S sources:

$$\mathbf{x}_i = \sum_{s=1}^S a_s \frac{1}{\sqrt{2\pi}\sigma_s^2} e^{-\frac{d(p_i, c_s)^2}{2\sigma_s^2}} \vec{v}_s \quad (4)$$

Here, d measures the Euclidean distance between the 3D position of the source location p_i and the center of active sources c_s . To generate the measurements $\mathbf{y} = \mathbf{L}\mathbf{x} + \epsilon$, the brain activation is projected onto sensor space using the lead field matrices \mathbf{L} described in the previous section. To introduce realistic challenges, zero-mean Gaussian noise $\epsilon \sim \mathcal{N}(0, \sigma_{\text{Noise}}^2 I)$ with varying signal-to-noise ratios (SNR), ranging from 0 dB to 30 dB, is applied to the measurements. More precisely, the noise standard deviation is given by:

$$\sigma_{\text{Noise}} = \frac{\sigma_{\text{Signal}}}{\sqrt{10^{\text{SNR}}}}. \quad (5)$$

This leads to the following hyperparameter that influences the generation:

- **Number of Activation** N_{Activ} : Ranges from 1 to 20, enabling simulation of varying source complexity.
- **Source Width** (σ): Spans from 10 mm to 80 mm, governing the spatial extent of each source activation, allow for simulating both diffuse and localized activity.
- **SNR**: Varied between 0 dB and 30 dB to introduce realistic noise levels and challenge the model's ability

to reconstruct sources under different signal quality conditions.

This approach ensures a diverse dataset for training and evaluation. Fig. 2 illustrates the variety of generated source patterns.

C. Evaluation Metrics

To evaluate the performance, we use the following three metrics, each investigating a different aspect of our prediction. The Normalized Mean Squared Error compares the voxel wise prediction, considering both amplitude and orientation, while the Earth Mover Distance considers also spatial distances of the prediction. Lastly, as we consider free-orientated sources, we evaluate the angular accuracy of the predicted sources.

1) *Normalized Mean Squared Error*: Given the ground truth sources \mathbf{x} and predicted sources $\hat{\mathbf{x}}$, the Normalized Mean Squared Error (NMSE) measures the voxel- and direction-wise deviation normalized by the total activation of the ground truth:

$$\text{NMSE}(\mathbf{x}, \hat{\mathbf{x}}) = \frac{\sum_{i=0}^N \|\mathbf{x}_i - \hat{\mathbf{x}}_i\|_2^2}{\sum_{i=0}^N \|\mathbf{x}_i\|_2^2} \quad (6)$$

By normalizing with the total activation, data samples with overall strong and weak brain activation are considered equally important along the validation dataset.

2) *Normalized Earth Mover's Distance*: To incorporate the spatial arrangement of brain sources and penalize larger misplacement of activations, Haufe et al. [61] proposed the use of the Earth Mover's Distance (EMD) [62]. It measures the minimal transport needed to align the predicted and real source distributions, thereby capturing the location error. To unify different simulation settings, we propose to normalize the EMD by the EMD of the ground truth and an uniform distribution. To compute the EMD, we use the publicly available POT package [63].

3) *Weighted Cosine Distance*: We consider free orientated sources and need to measure whether the models achieve good angular precision. Therefore, we compute the cosine distance at active source location between the ground truth and estimated activations.

$$\text{WCos}(\mathbf{x}, \hat{\mathbf{x}}) = 1 - \sum_i^N W_i \frac{\mathbf{x}_i^\top \cdot \hat{\mathbf{x}}_i}{\|\mathbf{x}_i\|_2 \|\hat{\mathbf{x}}_i\|_2} \quad (7)$$

The weight matrix $W_i = \frac{\|\mathbf{x}_i\|_2}{\sum_i \|\mathbf{x}_i\|_2}$ filters out non-active voxels and scales the importance proportional to the activation strength of the ground truth.

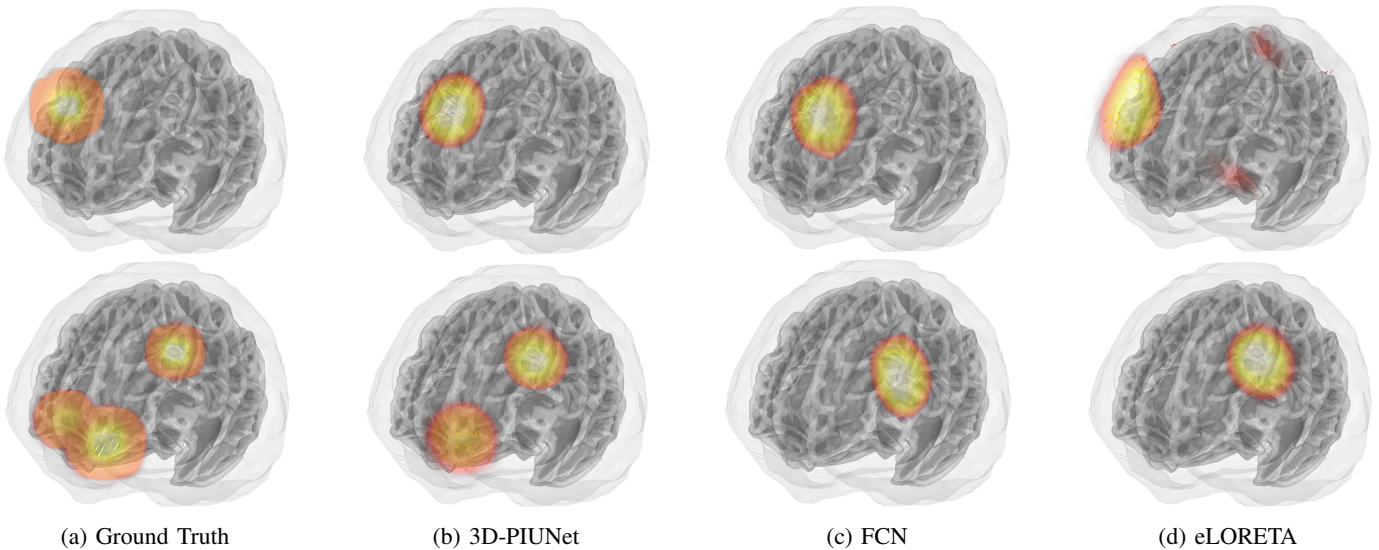


Fig. 3: The ground truth activation and reconstruction from 3D-PIUNet, the fully connected Network and eLORETA for **top** a single active source with SNR of 0dB and **bottom** 3 active sources with SNR of 40dB. 3D-PIUNet incorporates the learned data prior and refines the shape of an active region to match the ground truth. When multiple sources are active, it does focus on the strongest sources, missing weak activations in other parts of the brain.

D. Baselines

As a neural network competitor, we consider a fully connected network (FCN) with 4 fully connected layers and ReLU activation, upscaling the design of previous work [53]. The first layer maps from the 61 measurements to 1024 hidden dimensions, followed by two hidden layers with same dimensionality. The last layer maps from the 1024 hidden dimensions to $4819 \times 3 = 14457$ output channel. Note that this simple architecture already has around 17 million parameters, more than the 11 million parameters of 3D-PIUNet. We investigate different architecture sizes in Section V-F.

As classical baselines, we use eLORETA [10] as a minimum norm solution. Additionally, we compare against Lasso [20] with a group lasso penalty across three spatial dimensions, although we expect sparse methods to perform poorly with wide sources. Hyperparameters for these methods are optimized on the training data via a grid search.

V. EXPERIMENTS

In this section, we evaluate 3D-PIUNet on different synthetic settings to discover its advantages and limitations.

A. Visual Results

In Fig. 3, we visually compare source predictions for eLORETA and 3D-PIUNet for a single active source with 20mm extent reconstructed from single timestep EEG measurements for a single active source with 0dB noise (top) and three active sources with 40db noise (bottom). 3D-PIUNet reconstruction demonstrates a clear refinement of the eLORETA solution, more accurately capturing the spatial extent and peak activation of the ground truth.

B. Effect of Signal to Noise Ratio

In this experiment, we systematically vary the SNR from high noise setting with 0dB to nearly noise-free observations of 40dB. The results are depicted in Fig. 4. We evaluated reconstruction performance using proposed metrics from section IV-C: Earth Mover’s Distance (EMD) to quantify differences in spatial distributions, Mean Squared Error (MSE) for overall amplitude accuracy, and weighted cosine similarity to assess orientation similarity. Both neural network-based approaches (FCN and 3D-PIUNet) consistently outperform eLORETA across all metrics and SNR levels. Notably, 3D-PIUNet exhibited superior performance compared to the FCN, particularly at SNR levels above 10 dB. This suggests that the U-Net architecture, with its ability to learn complex spatial patterns and non-linear relationships, is better equipped to leverage the additional information available in higher SNR data.

C. Size of Sources

In Fig. 5, we show model performance on different-sized sources for a single active source with an SNR of 20dB. 3D-PIUNet improves on the solution of eLORETA and outperforms the Fully Connected Network with respect to all metrics. For small active sources with an extent of 10mm, we observe a low EMD, indicating that 3D-PIUNet predicts activation close to the correct source, even outperforming the sparse method Lasso. However, the high Normalized MSE suggests that none of the approaches perfectly matches the source on a voxel level. This trade-off may arise from the model’s focus on accurately localizing sources, even when their exact amplitude is harder to capture at this resolution. Notably, 3D-PIUNet demonstrates robustness to variations in source extent, effectively handling both sparse and spread sources despite being trained on a

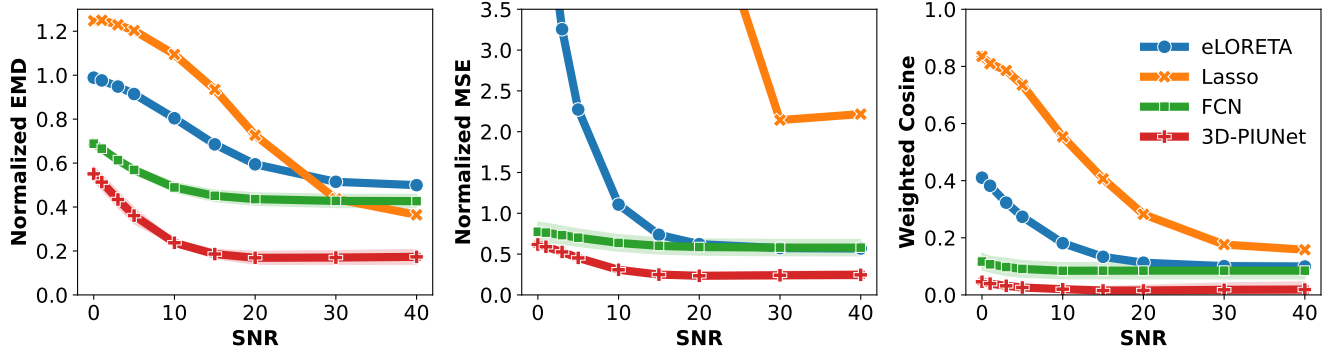


Fig. 4: Evaluation on the validation set across different Signal-to-Noise Ratios (SNR). The shaded area represents the standard deviations calculated from 5 trained models, emphasizing the consistency and reliability of the observed trends. **Left:** Normalized EMD decreases as SNR increases, with 3D-PIUNet consistently showing the lowest values, indicating superior performance in minimizing distribution discrepancies. **Center:** For low SNR, both neural network approaches substantially outperform eLORETA. The discrepancy shrinks as SNR increases, with 3D-PIUNet consistently achieving lower mean squared error. **Right:** Weighted Cosine Distance remains high across all SNR levels for the neural networks, suggesting robust similarity in orientation, while eLORETA shows a significant improvement with increasing SNR.

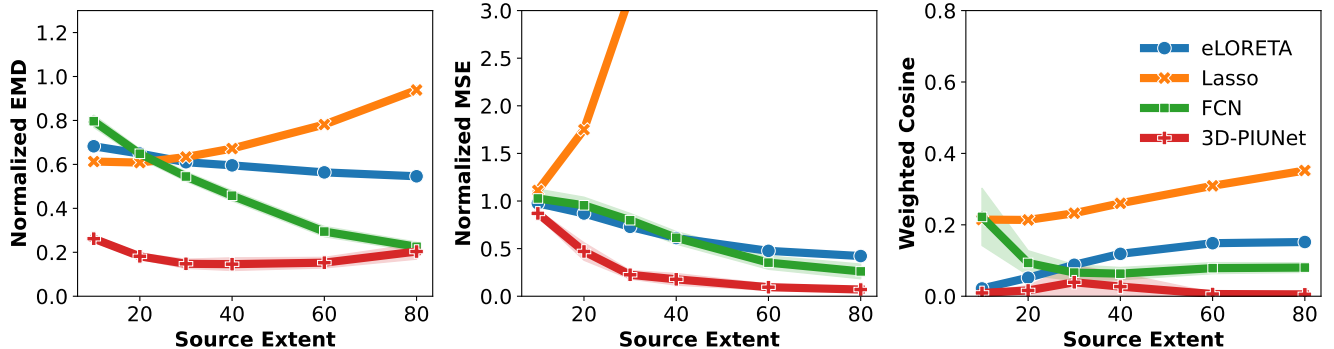


Fig. 5: 3D-PIUNet outperforms all baselines for different spatial extent of a single source with 5dB noise.

general dataset. This suggests the model has learned a versatile representation of source activity patterns.

D. Number of Sources

In Fig. 6, we analyze model performance for different numbers of active sources for the medium noise setting of 20dB and sources with random extent between 10 and 80mm. 3D-PIUNet consistently outperforms the FCN across all metrics, but shows a decrease in performance as the number of sources increases, particularly in terms of the normalized EMD. Interestingly, the performance of eLORETA remains relatively constant regardless of the number of active sources. This is likely because eLORETA is a linear method that distributes the estimated source activity smoothly across the entire source space. As the number of sources increases, eLORETA continues to spread the activity, leading to a consistent but less accurate reconstruction compared to the neural network models, which can learn more complex, non-linear relationships between sources and sensor data. As we consider only a single time step the signal of the sources overlap and the demixing becomes a very hard task, even when a data prior is learned. In future work, we aim to add the time dimension with varying source

amplitudes, providing additional information necessary for separating the different regions.

E. Transferability to Real Data

Using the pretrained model from last sections, we validate 3D-PIUNet on real data, utilizing the THINGS-EEG2 dataset [64]. This large-scale visual dataset followed the Rapid Serial Visual Presentation (RSVP) paradigm [65], [66] where images are displayed for 100 ms each, followed by a 100 ms blank screen in a series of 20 images. As the full dataset is large, we focus on the test set of subject 10, containing 20 trials of EEG recording for each image stimulus. We applied multivariate noise normalization [67], following the original work.

The THINGS-EEG2 dataset does not include MRI data for the subjects. Consequently, we use the same head geometry from section IV-A and recomputing the forward and pseudo-inverse for the new sensor layout. To enhance the signal-to-noise ratio, we apply ensemble averaging [68], combining EEG signals from 20 instances where the same image was presented to the subject. We apply eLORETA and 3D-PIUNet, to the preprocessed EEG data to estimate the source activations. As both are only spatial models, we predict for each time step

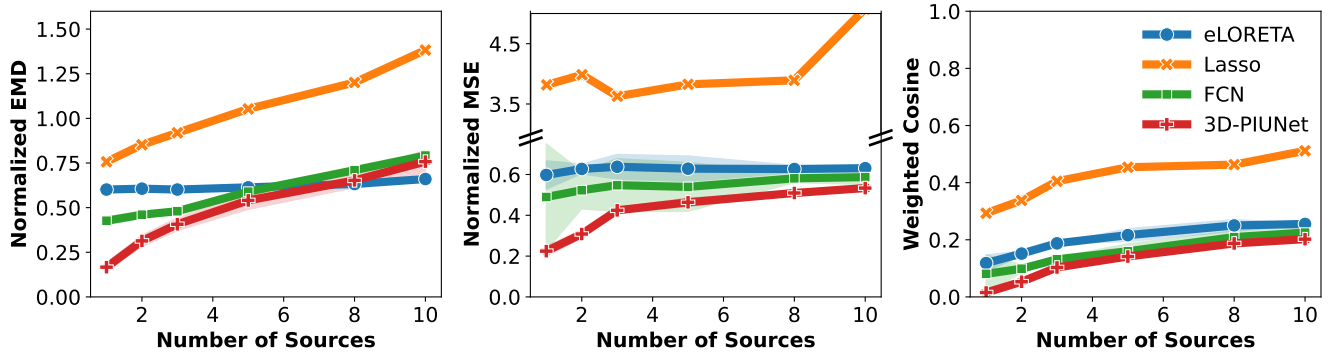


Fig. 6: We show the performance of increasing number of sources for 20dB Noise with varying extension. Even though the performance drops with more than 3 active regions, 3D-PIUNet remains superior to the other methods for up to 5 active sources.

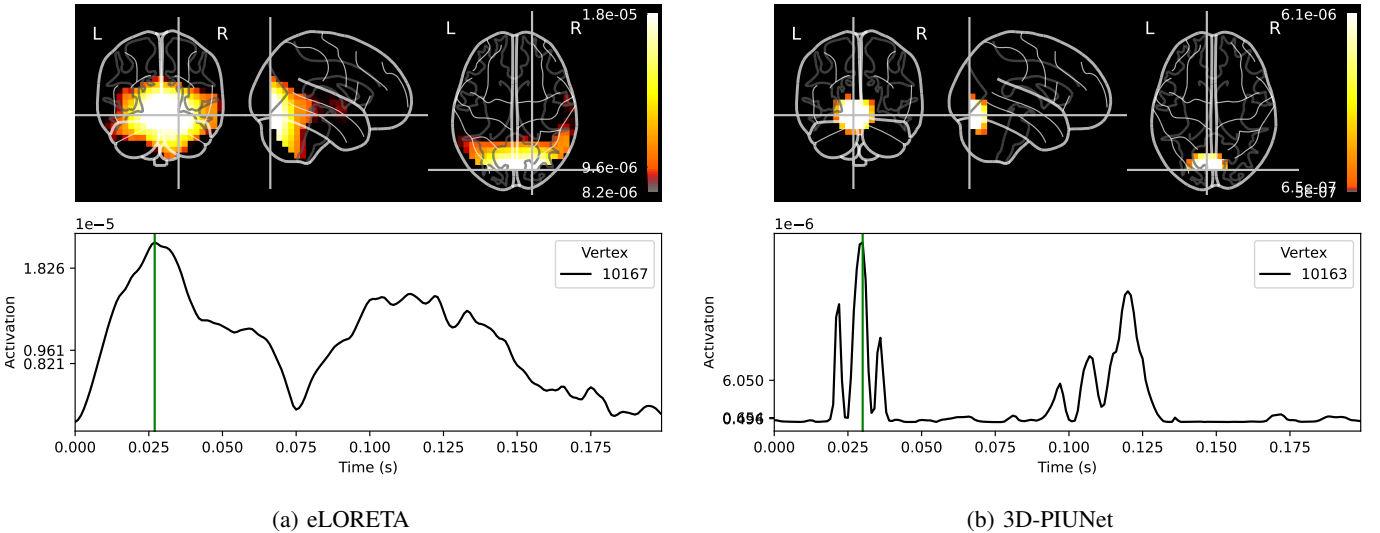


Fig. 7: This figure illustrates the predicted source activation for 20 ensemble stimuli from the THINGS-EEG dataset. Both panels display activation peaks of approximately 30 ms and around 110 ms post-stimulus exposure. In panel (a), the eLORETA solution shows a diffuse activation pattern, indicating a broader but less specific response within the visual cortex. In contrast, panel (b) demonstrates that 3D-PIUNet predicts localized and concentrated activation, specifically highlighting the visual cortex region. Additionally, the temporal response in eLORETA appears smoother and less defined, whereas 3D-PIUNet provides sharper, more distinct activation peaks, suggesting its superior ability to pinpoint the precise timing of neural activations.

independently. Note that 3D-PIUNet is trained only on the artificial data and applied to the different sensor layout without any fine-tuning by replacing just the pseudo inverse.

The predicted source activation of a single image condition is shown in Fig. 7. We observe two main activations in the visual cortex, the first around 30 ms and the second 130 ms after stimulus exposure. As the experiments follow the RSVP paradigm, we assume, that the first peak corresponds to the previous image while the peak around 130 ms is consistent with the image correlation results from the original paper [64].

The spatial and temporal characteristics of the activations differ significantly between the two methods. For eLORETA, the spatial activation pattern appears diffuse, while 3D-PIUNet is more localized, precisely highlighting the visual cortex. This concentrated activation suggests that 3D-PIUNet is better at pinpointing specific regions of neural activity. Additionally, the temporal response of eLORETA is smoother and less defined.

While this can be beneficial for capturing sustained neural activity, it might miss rapid changes or peaks in activation. Despite being trained only on a single time step synthetic data, 3D-PIUNet provides sharper, more distinct activation peaks, indicating a superior ability to detect precise timing of neural responses, which is crucial for understanding fast neural dynamics. It also matches the expected visually evoked potential [69], showing three distinct peaks around 100 ms after stimulus. This verifies the effectiveness of the proposed method also for real-world data.

F. Computational Efficiency

While 3D-PIUNet offers superior reconstruction accuracy, it is important to consider its computational demands. Training 3D-PIUNet requires approximately 5 hours on a single A100 GPU, compared to 2 hours for the FCN. However, the primary

TABLE I: Comparison of different model configurations with respect to runtime and EMD for 200 single source activations with 20 dB SNR and varying source extent. While 3D-PIUNet is slower than the Fully Connected Network, its runtime is still an order of magnitude faster than the iterative method Lasso.

Model	Depth	Width	Parameter	Runtime	EMD
eLORETA	3	1005	0.0 Mio	0.010s	0.60
Lasso	0	0	0.1 Mio	21.645s	0.70
FCN	3	512	8.0 Mio	0.006s	0.50
FCN	3	1024	17.0 Mio	0.004s	0.44
FCN	4	1024	18.0 Mio	0.004s	0.46
FCN	3	4096	93.0 Mio	0.003s	0.33
FCN	3	16384	774.0 Mio	0.003s	0.30
3D-PIUNet	3	8	0.7 Mio	0.191s	0.17
3D-PIUNet	3	32	11.1 Mio	0.415s	0.17
3D-PIUNet	4	32	19.1 Mio	0.866s	0.16
3D-PIUNet	3	64	44.2 Mio	2.192s	0.16

concern for practical applications is inference time. In our evaluation on a validation set of 200 samples (Table I), both eLORETA and the Fully Connected Network perform inference for 200 samples in a fraction of seconds. 3D-PIUNet, while slower, still completed inference in less than a second, notably faster than Lasso. While scaling up the FCN improves its performance, there remains a big gap even to the smallest version of 3D-PIUNet, demonstrating the parameter efficiency of the convolutional network.

VI. DISCUSSION & CONCLUSION

Inverse problems such as source localization are notoriously hard to solve due to their ill-posed nature. While end-to-end learning models such as neural networks have contributed to the recent progress in the field, we propose the hybrid approach, 3D-PIUNet, which combines the strengths of physics-based modeling and deep learning. 3D-PIUNet combines a not-learned physics-based pseudo-inverse with a learned 3D convolutional network operating directly in source space. This synergy achieves significant performance gains, even when using a standard head model. Our results demonstrate enhanced reconstruction accuracy and noise robustness compared to current state-of-the-art methods, effectively predicting both sparse and extended sources without requiring specific training for different types. This advancement could provide deeper insights into brain function and pave the way for improvements in clinical applications, such as diagnosing neurological disorders.

A. Limitations & Future Work

The quality of the data prior highly depends on the simulation used to train the model. While we used a diverse simulation setting, varying size and number of the sources, we impose a Gaussian prior on the source shape, which could be replaced by more realistic assumptions to refine the prior in future work. Additionally, incorporating known correlation structures between sources could further improve the learned prior.

Furthermore, our focus on the spatial aspects of source localization neglects temporal dynamics. As the information contained in a single measurement is limited, incorporating the

time domain could further improve the accuracy, especially in distinguishing multiple active sources. However, the proposed hybrid approach is general and the core idea of combining pseudo-inverse with deep learning can be adapted to also include the time domain, which is a direction we plan to pursue in future work.

Like many advanced learning approaches, the proposed 3D-PIUNet presents challenges in interpretability. Neural networks, while highly effective, can sometimes be seen as “black boxes”. In future research, we aim to integrate the recent advances on neural network explainability [70] to enhance the transparency and reliability of neural network-based source localization methods.

REFERENCES

- [1] C. M. Michel, M. M. Murray *et al.*, “EEG source imaging,” *Clinical neurophysiology*, vol. 115, no. 10, pp. 2195–2222, 2004.
- [2] B. He, A. Sohrabpour *et al.*, “Electrophysiological source imaging: a noninvasive window to brain dynamics,” *Annual review of biomedical engineering*, vol. 20, no. 1, pp. 171–196, 2018.
- [3] S. Baillet, J. C. Mosher, and R. M. Leahy, “Electromagnetic brain mapping,” *IEEE Signal processing magazine*, vol. 18, no. 6, pp. 14–30, 2001.
- [4] M. S. Hämäläinen and R. J. Ilmoniemi, “Interpreting magnetic fields of the brain: minimum norm estimates,” *Medical & biological engineering & computing*, vol. 32, pp. 35–42, 1994.
- [5] T. Delatolas, M. Antonakakis *et al.*, “EEG source analysis with a convolutional neural network and finite element analysis,” in *2023 45th Annual International Conference of the IEEE Engineering in Medicine & Biology Society (EMBC)*. IEEE, 2023, pp. 1–4.
- [6] R. Sun, A. Sohrabpour *et al.*, “Deep neural networks constrained by neural mass models improve electrophysiological source imaging of spatiotemporal brain dynamics,” *Proceedings of the National Academy of Sciences*, vol. 119, no. 31, p. e2201128119, 2022.
- [7] L. Hecker, R. Rupprecht *et al.*, “Convdp: A convolutional neural network for better EEG source imaging,” *Frontiers in Neuroscience*, vol. 15, p. 569918, 2021.
- [8] A. W. Thomas, H. R. Heekeren *et al.*, “Analyzing neuroimaging data through recurrent deep learning models,” *Frontiers in neuroscience*, vol. 13, p. 1321, 2019.
- [9] R. Sun, W. Zhang *et al.*, “Deep learning based source imaging provides strong sublobar localization of epileptogenic zone from MEG interictal spikes,” *NeuroImage*, vol. 281, p. 120366, 2023.
- [10] R. D. Pascual-Marqui, “Discrete, 3d distributed, linear imaging methods of electric neuronal activity. part 1: exact, zero error localization,” *arXiv preprint arXiv:0710.3341*, 2007.
- [11] A. Tarantola, *Inverse problem theory and methods for model parameter estimation*. SIAM, 2005.
- [12] M. Scherg and D. Von Cramon, “Two bilateral sources of the late AEP as identified by a spatio-temporal dipole model,” *Electroencephalography and Clinical Neurophysiology/Evoked Potentials Section*, vol. 62, no. 1, pp. 32–44, 1985.
- [13] M. Scherg, “Fundamentals of dipole source potential analysis,” *Auditory evoked magnetic fields and electric potentials. Advances in audiology*, vol. 6, no. 40-69, p. 25, 1990.
- [14] C. M. Michel and B. He, “EEG source localization,” *Handbook of clinical neurology*, vol. 160, pp. 85–101, 2019.
- [15] F.-H. Lin, T. Witzel *et al.*, “Assessing and improving the spatial accuracy in MEG source localization by depth-weighted minimum-norm estimates,” *NeuroImage*, vol. 31, no. 1, pp. 160–171, 2006.
- [16] A. M. Dale, A. K. Liu *et al.*, “Dynamic statistical parametric mapping: combining fMRI and MEG for high-resolution imaging of cortical activity,” *Neuron*, vol. 26, no. 1, pp. 55–67, 2000.
- [17] R. D. Pascual-Marqui, C. M. Michel, and D. Lehmann, “Low resolution electromagnetic tomography: a new method for localizing electrical activity in the brain,” *International Journal of psychophysiology*, vol. 18, no. 1, pp. 49–65, 1994.
- [18] R. D. Pascual-Marqui *et al.*, “Standardized low-resolution brain electromagnetic tomography (sLORETA): technical details,” *Methods Find Exp Clin Pharmacol*, vol. 24, no. Suppl D, pp. 5–12, 2002.

- [19] G. Pellegrino, T. Hedrich *et al.*, “Accuracy and spatial properties of distributed magnetic source imaging techniques in the investigation of focal epilepsy patients,” *Human brain mapping*, vol. 41, no. 11, pp. 3019–3033, 2020.
- [20] R. Tibshirani, “Regression shrinkage and selection via the lasso,” *Journal of the Royal Statistical Society Series B: Statistical Methodology*, vol. 58, no. 1, pp. 267–288, 1996.
- [21] K. Matsuura and Y. Okabe, “Selective minimum-norm solution of the biomagnetic inverse problem,” *IEEE Transactions on Biomedical Engineering*, vol. 42, no. 6, pp. 608–615, 1995.
- [22] S. Haufe, R. Tomioka *et al.*, “Large-scale EEG/MEG source localization with spatial flexibility,” *NeuroImage*, vol. 54, no. 2, pp. 851–859, 2011.
- [23] M. E. Tipping, “Sparse Bayesian learning and the relevance vector machine,” *Journal of Machine Learning Research*, vol. 1, no. Jun, pp. 211–244, 2001.
- [24] D. P. Wipf and S. S. Nagarajan, “Sparse estimation using general likelihoods and non-factorial priors,” in *Advances in Neural Information Processing Systems*, 2009, pp. 2071–2079.
- [25] A. Hashemi, C. Cai *et al.*, “Unification of sparse bayesian learning algorithms for electromagnetic brain imaging with the majorization minimization framework,” *NeuroImage*, vol. 239, p. 118309, 2021.
- [26] C. Cai, A. Hashemi *et al.*, “Robust estimation of noise for electromagnetic brain imaging with the Champagne algorithm,” *NeuroImage*, vol. 225, p. 117411, 2021.
- [27] A. Hashemi, C. Cai *et al.*, “Joint learning of full-structure noise in hierarchical bayesian regression models,” *IEEE Transactions on Medical Imaging*, 2022.
- [28] R. A. Chowdhury, J. M. Lina *et al.*, “MEG source localization of spatially extended generators of epileptic activity: comparing entropic and hierarchical bayesian approaches,” *PLoS one*, vol. 8, no. 2, p. e55969, 2013.
- [29] Y. Roy, H. Banville *et al.*, “Deep learning-based electroencephalography analysis: a systematic review,” *Journal of neural engineering*, vol. 16, no. 5, p. 051001, 2019.
- [30] P. Sanz Leon, S. A. Knock *et al.*, “The virtual brain: a simulator of primate brain network dynamics,” *Frontiers in neuroinformatics*, vol. 7, p. 10, 2013.
- [31] M. Breakspear, “Dynamic models of large-scale brain activity,” *Nature neuroscience*, vol. 20, no. 3, pp. 340–352, 2017.
- [32] D. Pantazis and A. Adler, “MEG source localization via deep learning,” *Sensors*, vol. 21, no. 13, p. 4278, 2021.
- [33] G. Huang, K. Liu *et al.*, “Electromagnetic source imaging via a data-synthesis-based convolutional encoder–decoder network,” *IEEE Transactions on Neural Networks and Learning Systems*, 2022.
- [34] M. Jiao, S. Yang *et al.*, “Multi-modal electrophysiological source imaging with attention neural networks based on deep fusion of EEG and MEG,” *IEEE Transactions on Neural Systems and Rehabilitation Engineering*, 2024.
- [35] J. Thomas, J. Jin *et al.*, “Automated detection of interictal epileptiform discharges from scalp electroencephalograms by convolutional neural networks,” *International journal of neural systems*, vol. 30, no. 11, p. 2050030, 2020.
- [36] M. Jiao, G. Wan *et al.*, “A graph fourier transform based bidirectional long short-term memory neural network for electrophysiological source imaging,” *Frontiers in neuroscience*, vol. 16, p. 867466, 2022.
- [37] Z. Yu, A. Kachenoura *et al.*, “Electrophysiological brain imaging based on simulation-driven deep learning in the context of epilepsy,” *NeuroImage*, vol. 285, p. 120490, 2024.
- [38] B. Zhang, D. Li, and D. Wang, “DCT based multi-head attention-BiGRU model for EEG source location,” *Biomedical Signal Processing and Control*, vol. 93, p. 106171, 2024.
- [39] M. Raissi, P. Perdikaris, and G. E. Karniadakis, “Physics-informed neural networks: A deep learning framework for solving forward and inverse problems involving nonlinear partial differential equations,” *Journal of Computational Physics*, vol. 378, pp. 686–707, 2019.
- [40] S. Chmiela, A. Tkatchenko *et al.*, “Machine learning of accurate energy-conserving molecular force fields,” *Science advances*, vol. 3, no. 5, p. e1603015, 2017.
- [41] K. Nicoli, C. J. Anders *et al.*, “Physics-informed bayesian optimization of variational quantum circuits,” *Advances in Neural Information Processing Systems*, vol. 36, 2024.
- [42] K. H. Jin, M. T. McCann *et al.*, “Deep convolutional neural network for inverse problems in imaging,” *IEEE transactions on image processing*, vol. 26, no. 9, pp. 4509–4522, 2017.
- [43] C. M. Hyun, H. P. Kim *et al.*, “Deep learning for undersampled MRI reconstruction,” *Physics in Medicine & Biology*, vol. 63, no. 13, p. 135007, 2018.
- [44] A. Gramfort, M. Luessi *et al.*, “MNE software for processing MEG and EEG data,” *NeuroImage*, vol. 86, pp. 446–460, 2014.
- [45] Y. LeCun, Y. Bengio, and G. Hinton, “Deep learning,” *Nature*, vol. 521, no. 7553, pp. 436–444, 2015.
- [46] O. Ronneberger, P. Fischer, and T. Brox, “U-net: Convolutional networks for biomedical image segmentation,” in *Medical Image Computing and Computer-Assisted Intervention–MICCAI 2015: 18th International Conference, Munich, Germany, October 5–9, 2015, Proceedings, Part III 18*. Springer, 2015, pp. 234–241.
- [47] A. Q. Nichol and P. Dhariwal, “Improved denoising diffusion probabilistic models,” in *International Conference on Machine Learning*. PMLR, 2021, pp. 8162–8171.
- [48] Y. Wu and K. He, “Group normalization,” in *Proceedings of the European conference on computer vision (ECCV)*, 2018, pp. 3–19.
- [49] S. Elfving, E. Uchibe, and K. Doya, “Sigmoid-weighted linear units for neural network function approximation in reinforcement learning,” *Neural networks*, vol. 107, pp. 3–11, 2018.
- [50] K. He, X. Zhang *et al.*, “Deep residual learning for image recognition,” in *Proceedings of the IEEE conference on computer vision and pattern recognition*, 2016, pp. 770–778.
- [51] A. Vaswani, N. Shazeer *et al.*, “Attention is all you need,” *Advances in neural information processing systems*, vol. 30, 2017.
- [52] A. Dosovitskiy, L. Beyer *et al.*, “An image is worth 16x16 words: Transformers for image recognition at scale,” *arXiv preprint arXiv:2010.11929*, 2020.
- [53] L. Hecker, R. Rupprecht *et al.*, “Long-short term memory networks for electric source imaging with distributed dipole models,” *bioRxiv*, 2022.
- [54] D. P. Kingma and J. Ba, “Adam: A method for stochastic optimization,” *arXiv preprint arXiv:1412.6980*, 2014.
- [55] M. Fuchs, J. Kastner *et al.*, “A standardized boundary element method volume conductor model,” *Clinical neurophysiology*, vol. 113, no. 5, pp. 702–712, 2002.
- [56] A. Gramfort, M. Luessi *et al.*, “MEG and EEG data analysis with MNE-Python,” *Frontiers in Neuroscience*, vol. 7, no. 267, pp. 1–13, 2013.
- [57] B. Fischl, M. I. Sereno *et al.*, “High-resolution intersubject averaging and a coordinate system for the cortical surface,” *Human brain mapping*, vol. 8, no. 4, pp. 272–284, 1999.
- [58] D. L. Colton and R. Kress, *Inverse acoustic and electromagnetic scattering theory*. Springer, 1998, vol. 93.
- [59] J. Kaipio and E. Somersalo, “Statistical inverse problems: discretization, model reduction and inverse crimes,” *Journal of computational and applied mathematics*, vol. 198, no. 2, pp. 493–504, 2007.
- [60] C. H. Wolters, S. Lew *et al.*, “Combined EEG/MEG source analysis using calibrated finite element head models,” *Biomedizinische Technik/Biomedical Engineering. Rostock, Germany: Walter de Gruyter*, vol. 55, no. Suppl 1, pp. 64–68, 2010.
- [61] S. Haufe, V. V. Nikulin *et al.*, “Combining sparsity and rotational invariance in EEG/MEG source reconstruction,” *NeuroImage*, vol. 42, no. 2, pp. 726–738, 2008.
- [62] Y. Rubner, C. Tomasi, and L. J. Guibas, “The earth mover’s distance as a metric for image retrieval,” *International journal of computer vision*, vol. 40, pp. 99–121, 2000.
- [63] R. Flamary, N. Courty *et al.*, “POT: Python optimal transport,” *Journal of Machine Learning Research*, vol. 22, no. 78, pp. 1–8, 2021.
- [64] A. T. Gifford, K. Dwivedi *et al.*, “A large and rich EEG dataset for modeling human visual object recognition,” *NeuroImage*, vol. 264, p. 119754, 2022.
- [65] H. Intraub, “Rapid conceptual identification of sequentially presented pictures,” *Journal of Experimental Psychology: Human Perception and Performance*, vol. 7, no. 3, p. 604, 1981.
- [66] T. Grootswagers, A. K. Robinson, and T. A. Carlson, “The representational dynamics of visual objects in rapid serial visual processing streams,” *NeuroImage*, vol. 188, pp. 668–679, 2019.
- [67] M. Guggenmos, P. Sterzer, and R. M. Cichy, “Multivariate pattern analysis for MEG: A comparison of dissimilarity measures,” *Neuroimage*, vol. 173, pp. 434–447, 2018.
- [68] L. Sörnmo and P. Laguna, “Chapter 4 - evoked potentials,” in *Bio-electrical Signal Processing in Cardiac and Neurological Applications*, ser. Biomedical Engineering. Burlington: Academic Press, 2005, pp. 181–336.
- [69] D. J. Creel, “Visually evoked potentials,” *Handbook of clinical neurology*, vol. 160, pp. 501–522, 2019.
- [70] W. Samek, G. Montavon *et al.*, “Explaining deep neural networks and beyond: A review of methods and applications,” *Proceedings of the IEEE*, vol. 109, no. 3, pp. 247–278, 2021.

APPENDIX

A. Network Architecture

We illustrate the network architecture of 3D-PIUNet in Fig. 8. The process begins with transforming EEG data into the source space using the pseudo-inverse \mathbf{L}^\dagger . This transformed data is then processed through a 3D convolutional U-Net architecture, an encoder-decoder network that comprises two primary computational components.

The first component is the Residual Block (depicted in blue), which integrates Group Normalization layers [48], SiLU activation functions [49], and $3 \times 3 \times 3$ convolutional layers. Within each spatial resolution stage, two Residual Blocks are applied both in the encoding, going down in resolution, and decoding, going up in resolution, phase. The decoder reduces the spatial resolution with a residual block of stride 2, initially from $32 \times 32 \times 32$ to $16 \times 16 \times 16$ and then to $8 \times 8 \times 8$ voxels. During each resolution reduction, the number of feature channels is doubled, starting from $C = 32$ and increasing to $4C = 128$ channels, thereby capturing increasingly abstract features at coarser resolutions. The decoder uses up-scaling residual blocks to map back to higher resolutions. At each resolution, a skip-connection appends the output of the encoding block with the same resolution to the upscaled features. This allows the lower levels to focus on abstract features, while high resolution details can be included directly from the encoder.

At the lowest resolution of $8 \times 8 \times 8$, a Spatial Attention Block (depicted in red) is introduced to enhance feature representation. This block employs three separate linear transformations via $1 \times 1 \times 1$ convolutions for each voxel, generating tensors that are then flattened along spatial dimensions. This process produces the query $Q \in \mathbb{R}^{8 \times 8 \times 8 \times 4C}$, key $K \in \mathbb{R}^{512 \times 128}$, and value $V \in \mathbb{R}^{512 \times 128}$ for the attention mechanism [51]. The attention operation involves computing the matrix product of the query and key, scaling by the square root of the key dimension $d_k = 128$, and applying a softmax function to generate the attention map. This map is used to weight the value matrix, thereby enabling each voxel to prioritize the most relevant information from other locations:

$$\text{Attention}(Q, K, V) = \text{softmax}\left(\frac{QK^\top}{\sqrt{d_k}}\right)V \quad (8)$$

The weighted value matrix is reshaped back into the 3D volume and is subsequently processed through a $1 \times 1 \times 1$ convolution for linear projection. The resulting feature maps are then added to the input of the attention block, effectively integrating contextual information from across the spatial domain.

By using these two blocks, the used architecture combines the benefits of parameter efficient local 3D convolutional filters and with the spatial attention for global information passing in reduced resolution.

B. Computing Normalized Earth Mover Distance

The Earth Mover Distance measures the distributional distance between predicted and true sources, capturing both the localisation and shape of the sources. By including the Euclidean distance $M_{ij} = \|p_i - p_j\|_2$ between source location i and j in 3D space, small location differences are weighted

less. However, to calculate the EMD, one needs to solve the constraint optimization problem:

$$\text{EMD}(\mathbf{x}, \hat{\mathbf{x}}) = \min_F \sum_i^N \sum_j^N F_{ij} M_{ij} \quad (9)$$

$$\text{s.t.} \quad F \geq 0; \quad \sum_j^n F_{ij} = \mathbf{x}_i^A; \quad \sum_i^n F_{ij} = \hat{\mathbf{x}}_j^A$$

$$\mathbf{x}_i^A = \frac{\|\mathbf{x}_i\|_2}{\sum_j^N \|\mathbf{x}_j\|_2}; \quad \hat{\mathbf{x}}_i^A = \frac{\|\hat{\mathbf{x}}_i\|_2}{\sum_j^N \|\hat{\mathbf{x}}_j\|_2}$$

Here, \mathbf{x}^A and $\hat{\mathbf{x}}^A$ are the normalized amplitudes of true and predicted source activations, respectively. To solve this optimization problem, we use the publicly available POT package [63]. As this metric varies with different simulation settings, we propose the normalized EMD by dividing the EMD with the EMD of the ground truth to an uniform distributed activation $\mathbf{u} = \frac{1}{N}\mathbf{1}$ spread equally along all potential sources:

$$\text{NEMD}(\mathbf{x}, \hat{\mathbf{x}}) = \frac{\text{EMD}(\mathbf{x}, \hat{\mathbf{x}})}{\text{EMD}(\mathbf{x}, \mathbf{u})} \quad (10)$$

This accounts for larger source activation areas due to multiple sources or large source extent, which would otherwise automatically produce lower EMD.

C. Different Loss Functions

In this section, we compare the proposed ℓ_1 loss with other losses commonly used in the literature. We evaluate the results on single-source prediction across three different noise levels, as shown in Fig. 9. For comparison, we also train our architecture using the ℓ_2 loss and cosine similarity loss [53] in source space. While these losses provide reasonable performance, the ℓ_1 loss consistently performs best. We also tested a reconstruction loss in the measurement space, typically optimized in classical methods:

$$\mathcal{L}_{rec}(\hat{x}, y) = \|\hat{\mathbf{x}} - \mathbf{x}\|_1 + \lambda_{rec} \|\mathbf{L}\hat{\mathbf{x}} - y\|_2^2 \quad (11)$$

The reconstruction term is weighted by a constant $\lambda_{rec} = 0.0001$ to compensate for different magnitudes. However, because the measurements are noisy, this loss drives the network's predictions away from the ground truth, degrading performance in high noise scenarios. Overall, our results indicate that the ℓ_1 loss in source space is the most effective for training the neural network.

D. Different Pseudo Initialization

In this section, we investigate the relevance of the pseudo-inverse solution for model performance by training a 3D convolutional network with different pseudo-inverse solutions as starting points. We compare the proposed eLORETA pseudo-inverse with minimum norm estimates (MNE), sLORETA, dSPM, and beamformer solutions implemented in the MNE package [44], as well as the Moore-Penrose inverse. Fig. 10 illustrates performance on single-source prediction across three different noise levels. While the performance of the regularized minimum norm solutions is similar, the eLORETA solution achieves the best results. The beamformer, however, shows

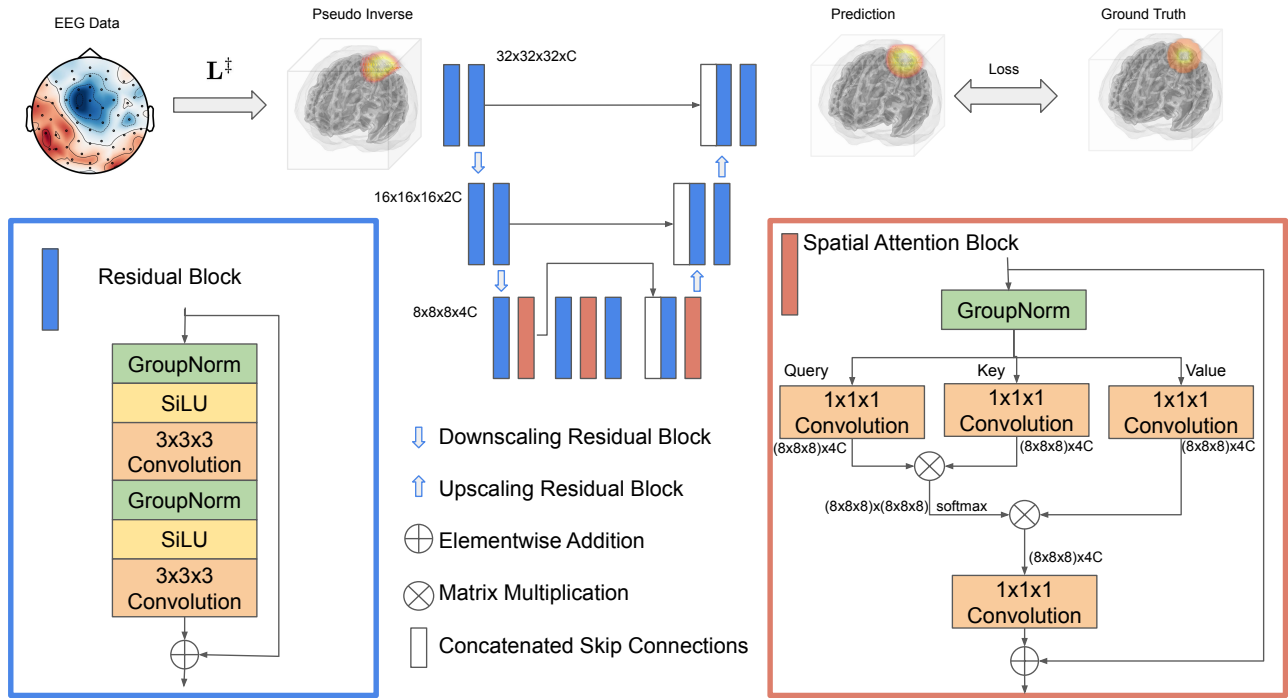


Fig. 8: An overview of the 3D-PIUNet architecture. First, the eLORETA pseudo inverse L^\dagger maps the EEG measurement to a 3D source space of $32 \times 32 \times 32$ resolution. Next, a series of 3D convolutional residual blocks encodes the pseudo-inverse down to an $8 \times 8 \times 8$ latent representation. The skip connections between the encoder and decoder allow the model to preserve high-resolution information. At the latent resolution, spatial attention blocks facilitate enhanced interactions between voxels.

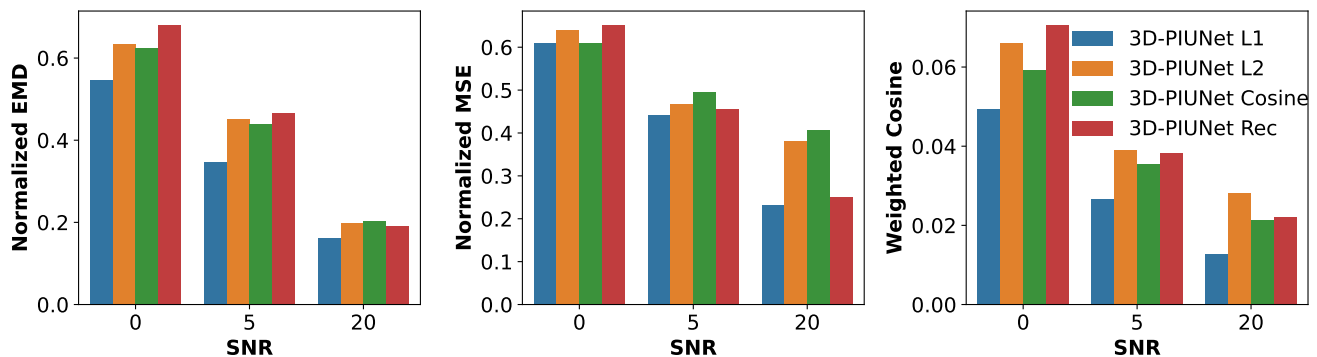


Fig. 9: Comparison of training 3D-PIUNet with different loss functions. The proposed ℓ_1 loss (blue) outperforms the ℓ_2 loss (orange), cosine similarity (green) and additional reconstruction loss (red) across all metrics and SNR levels.

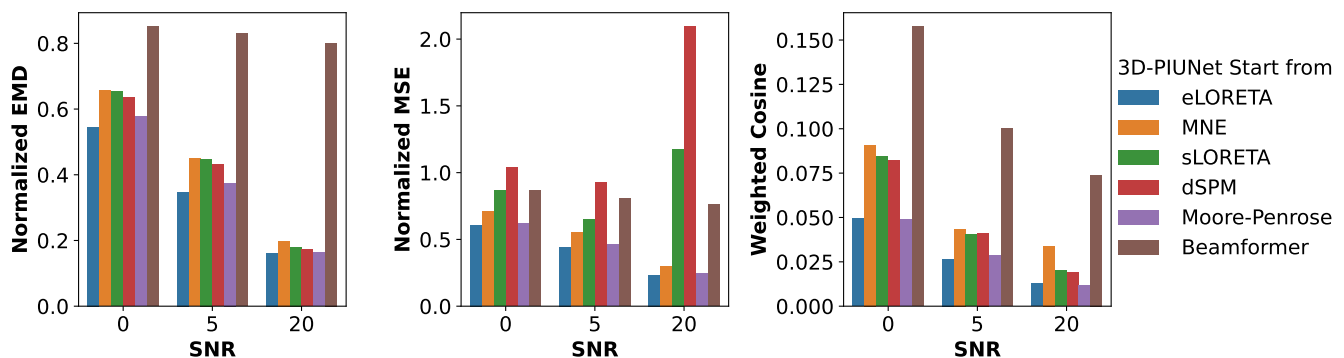


Fig. 10: Model performance when training the 3D Convolutional Network starting from different Pseudo Inverse solutions.

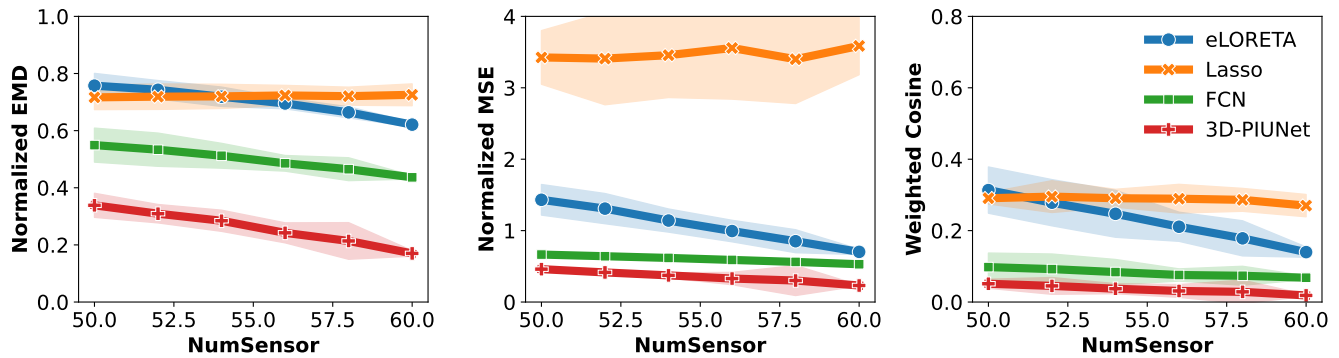


Fig. 11: We evaluate the model performance for a reduced set of sensors, by using only a subset of the 61 available sensors. While there is a small decrease in performance, 3D-PIUNet still performs best, demonstrating robustness to missing values.

reduced performance, likely due to its sensitivity to noise covariance estimation and source correlation, which can lead to suboptimal localization and model performance under varying SNR conditions. Overall, 3D-PIUNet demonstrates robust performance across different pseudo-inverse initializations, highlighting its adaptability and effectiveness regardless of the chosen inverse method.

E. Robustness to Missing Sensors

In this section, we evaluate the model’s robustness to missing sensor data. Starting with the original 61 sensors, we randomly set up to 11 sensor measurements and their corresponding entries in the lead field matrix to zero, simulating missing data. Given that the impact of missing sensors can vary depending on their locations, we plot the standard deviation of performance across five different random subsets of missing sensors. The results for a single active source with an SNR of 20dB are shown in Fig. 11. Both neural network approaches demonstrate greater robustness to missing sensor values compared to eLORETA, suggesting that the learned data priors effectively compensate for measurement errors and improve resilience to data loss.